Special Issue of the 6th International Congress & Exhibition (APMAS2016), Maslak, Istanbul, Turkey, June 1–3, 2016

In Situ Solution Process for Fabricating Thermally and Mechanically Stable Highly Conductive ZnO–CNT Fiber Composites

M.M. Hossain[a], S.B. Son[b] and J.R. Hahn[a,c,*]

[a]Department of Chemistry and Bioactive Material Sciences, Research Institute of Physics and Chemistry, Chonbuk National University, Jeonju 561-756, Korea

[b]Jeonju Center, Korea Basic Science Institute, Jeonju 561-756, Republic of Korea

[c]Textile Engineering, Chemistry and Science, North Carolina State University, 2401 Research Dr., Raleigh, NC 27695-8301, USA

A simple *in situ* solution process was developed to produce a mechanically and thermally stable ZnO–carbon nanotube fiber composite. ZnO nanoparticles were homogeneously deposited onto the surfaces of and interstices within CNT fibers (between individual CNTs). X-ray photoelectron spectroscopy and Raman analysis revealed that ZnO nanoparticles contained oxygen vacancy defects and CNT fibers included oxygen containing functional group that strongly interacted with Zn. The strong interaction enhanced the mechanical properties of the composite fibers. The Young modulus (20 GPa) and tensile strength (118 MPa) were enhanced compared to the corresponding values of the pristine CNT fibers. The thermal stability was high up to 880 °C and light absorption was enhanced across the UV to near IR region in a ZnO–CNT fiber composite. The electrical conductivity of the composite was high up to 954 S/cm despite semiconductor deposition.

DOI: 10.12693/APhysPolA.131.124

PACS/topics: 81.05.–t

1. Introduction

Fiber-shaped materials show promise as energy storage candidates. For example, woven textiles prepared from fiber-shaped solar cells or supercapacitors can provide a high degree of flexibility and low weight while offering solar absorption capabilities for electricity generation and a high conductivity for photoexcited electrons. Fiber-shaped materials are useful during electricity interruption, particularly in harsh environments. The use of fiber-shaped materials in flexible, lightweight and portable electronic devices has been extensively explored [1–6]. Fiber-shaped materials such as Kevlar [1], metal fibers [2], metal wires [3], carbon fibers [4], carbon nanotubes (CNTs) [5], or graphene [6] fiber have been explored for their utility. Polymer fibers have enabled significant breakthroughs in the fabrication of flexible devices although they tend to provide poor electrical conductivity or insulation properties [7, 8]. Metal wires have been explored as efficient electrodes in electronic devices due to their high electrical conductivities [9]; however, metal wires tend to be heavy, offer poor flexibility, and cannot be effectively woven into textiles.

The excellent mechanical and electrical conductivity properties [5, 10, 11] of CNT fibers have been widely studied. Dry or wet spinning processes [12] have been used to spin CNTs into fibers hundreds of meters in length and a few micrometers in width CNT fibers tend to exhibit relatively low electrocatalytic activities, which presents a significant barrier to their electronic applications. Furthermore, CNT fiber devices offer low efficiency photoelectric conversion and energy storage properties [5, 13]. The deposition of a variety of metal oxides (MnO_2 [14], NiO [15], RuO_2 [16], V_2O_5 [17], TiO_2 [3], ZnO [18]) or metal nanoparticles (Pt [19], PtRu [20], PtSn [21], Pd [22], Au [22], Ru [23], Ag [24]) onto the CNT fiber surfaces has been reported to improve the electrochemical and optical properties of CNT fibers. Metal oxides or metal nanoparticles are typically deposited randomly and inhomogeneously onto CNT fibers. The smooth deposition of metal or metal oxide nanoparticles is necessary for enhancing the electronic and optical properties of CNT fibers. Smooth deposition requires CNT pretreatment, CNT functionalization, CNT acid oxidation, surfactant introduction, or particular fabrication processes [19–24]. Unfortunately, the electrical conductivity of a CNT fiber typically decreases upon deposition of semiconductive nanoparticles onto the CNT surfaces.

Here we developed an *in situ* solution process for CNT fiber modification with ZnO nanoparticles. We previously reported the fabrication of ZnO/C core–shell nanorods through an *in situ* process [25, 26]. We modified that method to fabricate ZnO–CNT fiber composites that exhibited excellent mechanical and light absorption properties and a high electrical conductivity. ZnO was chosen because it is low in cost, environmentally friendly, provides strong photoinduced hole oxidation, and has a high electron mobility [27]. By incorporating ZnO into

*corresponding author; e-mail: jrhahn@jbnu.ac.kr

CNT fibers, we enhanced the mechanical properties and electrical conductivity of the fibers. Our *in situ* method was performed without the need for pretreatment, oxidation, or CNT functionalization steps. The individual CNTs and ZnO nanoparticles strongly interacted after thermal decomposition of a zinc acetate layer on the CNT fiber surfaces. The strong interaction enabled the smooth deposition of ZnO nanoparticles, enhanced the Young modulus and stress, enabled light absorption throughout the 300–2100 nm region and enhanced the thermal stability of the CNT fibers as compared to the pristine CNT fibers. The electrical conductivity did not decrease significantly upon ZnO deposition due to the strong interactions between Zn and the CNTs.

2. Experimental

2.1. Chemicals

Zinc acetate dihydrate (Sigma Aldrich, 99% purity) was used as a precursor material for the ZnO nanoparticles. Ethanol (Sigma Aldrich, 95%) was used as a solvent to prepare the zinc acetate dihydrate solution. Au wires (0.05 mm in diameter, 171105, Nilaco Co) and silver paste (Leit Silver, Sigma Aldrich) were used to measure the electrical conductivity of the CNT fibers and the ZnO–CNT fiber composite. CNT fibers were fabricated from acetone (99.5%, Daejung Chemicals and Metals), ferrocene (98% Sigma Aldrich) and thiophene (99%, Sigma Aldrich). The CNT fibers were concentrated using dimethyl sulfoxide (DMSO, 99.5%, Sigma Aldrich).

2.2. Instruments

Bath sonication was performed to prepare the zinc acetate dihydrate solution. The electrical conductivities of the CNT fibers and composite fibers were measured using a four-point probe combined with Keithley Instruments (2400 SourceMeter and 2000 MULTIMETER). The sample structures were analyzed using field emission scanning electron microscopy (FESEM, S-4700, Hitachi) and X-ray diffraction (XRD, Smart Lab, Rigaku). The samples were spectroscopically characterized by UV/vis/NIR spectrophotometry (V670, JASCO), the Raman spectroscopy (HORIBA JOBIN YVON, Lab RAM HR, Laser 514.54 and 632.817), and X-ray photoelectron spectroscopy (XPS, K-Alpha, Thermo Scientific). The mechanical properties were measured using a Universal Testing Machine (UTM 5567A, INSTRON). Focused ion beam (FIB) techniques were used to cut the CNT fibers, and energy dispersive X-ray (EDX) characterizations were performed using a HELIOS NANOLAB 650 (FEI).

2.3. Preparation of the CNT fibers

A liquid feedstock [28] containing acetone (a carbon source), ferrocene (0.2 wt%, a catalyst precursor), and thiophene (0.8 wt%, a promoter) was injected into a heated furnace at 1200 °C. The carrier gas was delivered at a rate of 1000 SCCM to synthesize continuous CNT fibers, as described previously [28]. The resulting continuous CNT array was then declined into a water tank and subsequently wound at a rate of 5 m/min. The CNT fibers were densified in DMSO followed by drying at 100 °C.

2.4. Fabrication of a ZnO–CNT fiber composites in situ

CNT fibers were mounted on a frame of stainless steel wire (Fig. 1a). Zinc acetate dihydrate (3 g) was dissolved in ethanol (50 ml, Fig. 1e) and sonicated for 1 h to produce a homogeneous solution (60 mg/ml) at room temperature. CNT fibers on the steel frame were positioned in a Petri dish (Fig. 1b), and the zinc acetate dihydrate solution was poured slowly into the dish. As crystals of zinc acetate formed in the solution (Fig. 1d), the steel frame was quickly removed from the solution and dried at 180 °C in a preheated furnace for 2 min to remove the ethanol solvent. The zinc acetate dihydrate solution in the dish was poured into a vial and sonicated again to dissolve any solid zinc acetate precipitate. As the solution became clear, the dried CNT fiber frame was placed into the solution again. A total of 3 or 4 cycles were applied to deposit the zinc acetate onto the CNT fiber surface. During each cycle, the fibers were immersed into the solution for 3 to 5 min. Long immersion times could permit the zinc acetate solution to penetrate the CNT fibers. It was important to avoid rapid precipitation onto the CNT fiber surfaces, however, as opposed to penetration of the fibers over long immersion times. A low lab temperature (10–15 °C) facilitated the effective penetration of the solution into the CNT fibers. Finally the zinc acetate deposited CNT fibers were placed in a preheated furnace (200 °C) and the temperature was slowly increased to 450 °C at a rate of 4 °C/min. The fibers were then heated at 450 °C for 20 min to decompose the zinc acetate to produce the ZnO–CNT fiber composite. Other samples of ZnO–CNT fiber composites were prepared at 350, 400, and 500 °C to investigate the effects of the temperature on the sample structure.

2.5. Fabrication of ZnO–CNT fiber composites ex situ

A zinc acetate solution (50 ml, 60 mg/ml in ethanol) in a round-bottom flask was stirred in a silicon oil bath for 2 h at 100 °C to produce ZnO nanoparticles. The CNT fibers mounted on a steel frame were immersed in a solution of ZnO nanoparticles for 30 min to produce a ZnO–CNT fiber composite. The composite was then removed and dried at 100 °C for 2 h to evaporate away the ethanol solvent.

2.6. Synthesis of the purified ZnO–CNT fiber composites

CNT fibers mounted on a glass slide were heated at 400 °C for 45 min to oxidize any metal impurities. After cooling, the heated CNT fibers were immersed in concentrated HCl. The CNT fibers in HCl were boiled at 80 °C for 4 h to remove metal impurities as metal chlorides. After boiling, the fibers were washed in DI water several

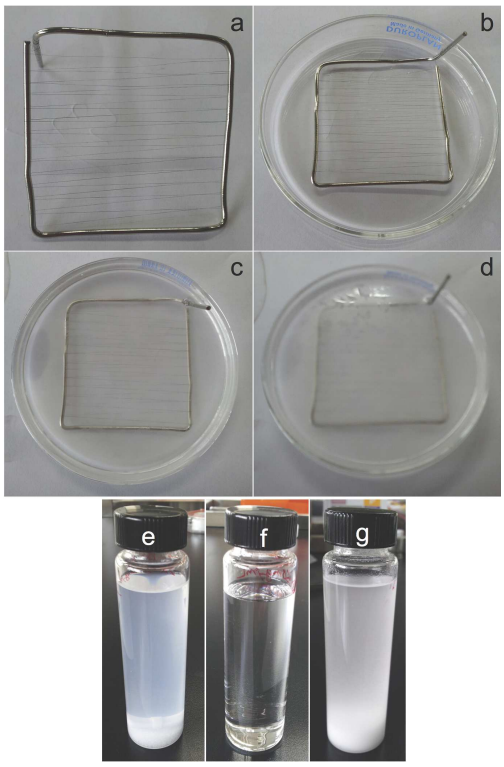

Fig. 1. (a) CNT fibers mounted on a frame of stainless steel wire. (b) CNT fibers on the frame were positioned in a Petri dish. (c) CNT fibers frame immersed in 60 mg/ml solution of zinc acetate. (d) Crystals of zinc acetate formed in the solution. (e) Zinc acetate in ethanol. (f) Zinc acetate solution after bath sonication. (g) Zinc acetate solution (60 mg/ml) after settling down for a few minutes.

times to remove any remaining impurities and were heated at 400 °C for 45 min. Finally, the purified CNT fibers were used to produce a ZnO–CNT fiber composite using the procedure described in Sect. 2.4.

3. Results and discussion

Figures 2a–2d show FESEM images of the ZnO–CNT fiber composites prepared on a Si wafer. Several CNT fibers are shown in Fig. 2a. The ZnO nanoparticles are apparent in the magnified views of the regions marked with rectangles (Fig. 2c,d). ZnO nanoparticles were deposited homogeneously with an average size of 50 nm. The aggregated ZnO nanoparticles on the CNT fibers appeared as large spheres in Fig. 2b and c. As described in Sect. 2, the ZnO–CNT fiber composites were synthesized from as-synthesized or purified CNT fibers. For comparison, FESEM images of the as-synthesized or purified CNTs were obtained, as shown in Fig. 2e and f, respectively. Purification was performed by heating and HCl treatment to remove metal impurities from CNT fiber. FESEM images of the as-synthesized CNT fibers revealed individual CNTs and clearly differed from the surface images of the ZnO–CNT fiber composites. After purifying the CNT fibers, the morphologies were characterized and found to be similar to those of the as-synthesized fibers, indicating that the CNT fibers were not damaged through heating and HCl treatment.

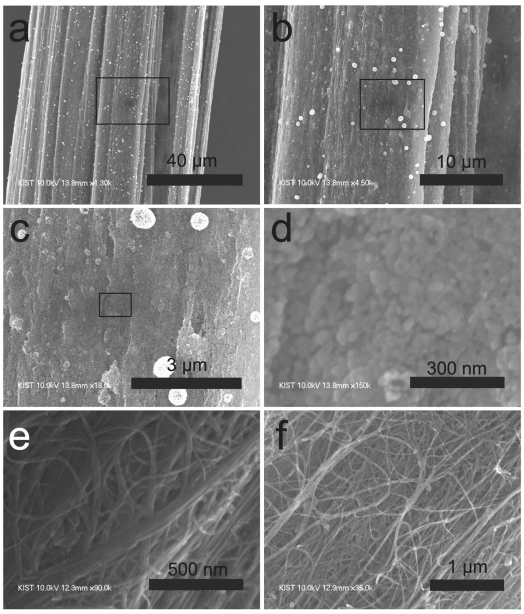

Fig. 2. SEM images of (a)–(d) ZnO–CNT fiber composites, (e) as-synthesized CNT fibers, and (f) CNT fibers after thermal and acid treatment, respectively. The ZnO nanoparticles were examined in greater detail by collecting magnified images of the rectangular regions shown in (a)–(c).

A synthetic scheme for obtaining the ZnO–CNT fiber composites is illustrated in Fig. 3. As-synthesized CNT fibers (Fig. 3a) (or purified CNT fibers) were coated with ZnO acetate (Fig. 3b) and then heated at 450 °C for 20 min to produce a ZnO–CNT fiber composite *in situ*. Onto the CNT fibers, ZnO nanoparticles and aggregated spheres formed (Fig. 3c). SEM images of the resulting fibers are displayed in Fig. 3. As a control experiment ZnO nanoparticles were deposited onto CNT fibers *ex situ* (refer to Sect. 2). Figure 4a and b presents SEM images of the *ex situ* prepared fiber composites, indicating that ZnO nanoparticles were not deposited homogeneously as in the *in situ* process.

The atomic structure of the ZnO–CNT fiber composite was analyzed by XRD. XRD spectra of the Si substrate, as-synthesized CNT fibers, ZnO–CNT fiber composites and pure ZnO nanoparticles were obtained (Fig. 5). The spectrum of the as-synthesized CNT fibers (Fig. 5a*b*) displayed peaks at 19.07 and 25.10 (marked by arrows). The peak at 25.10 arose from crystalline carbon whereas the peak at 19.07 corresponded to higher *d*-spacings in the poorly crystalline carbon. Higher *d*-spacings may have resulted from oxygen containing functional groups that increased the carbon layer–layer distance. The peaks marked by black squares in curve 5a*b* were attributed

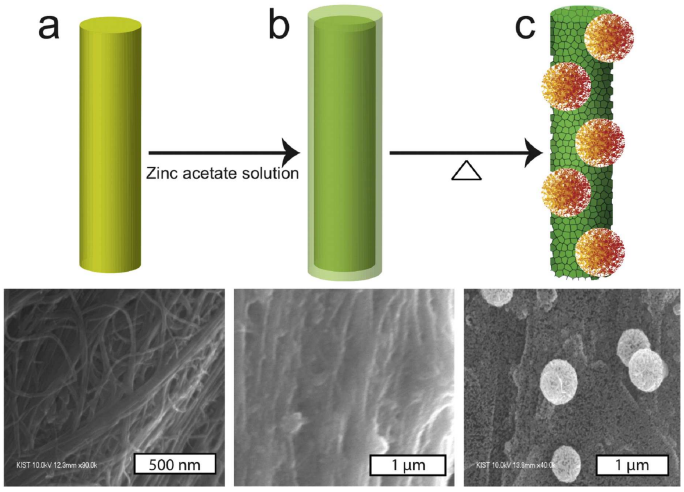

Fig. 3. Schematic diagram showing the fabrication of a ZnO–CNT fiber composite *in situ*. (a) An as-synthesized CNT fiber. (b) A zinc acetate-coated CNT fiber. (c) Thermal heating of the zinc acetate-coated CNT fibers led to the formation of the ZnO–CNT fiber composite. SEM images of the outer surfaces at each step are displayed.

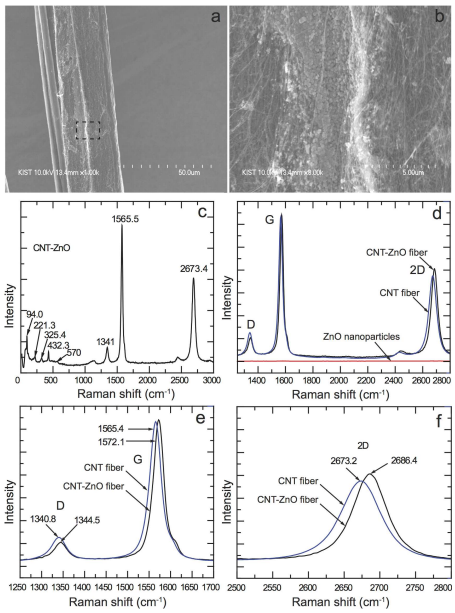

Fig. 4. (a) and (b) SEM images of the *ex situ* prepared ZnO–CNT fiber composites. (c) Raman spectrum collected from the *ex situ* prepared ZnO–CNT fiber composites. (d)–(f) Magnified spectra over the regions 1250–2800, 1250–1700, and 2500–2800 cm^{-1}, respectively.

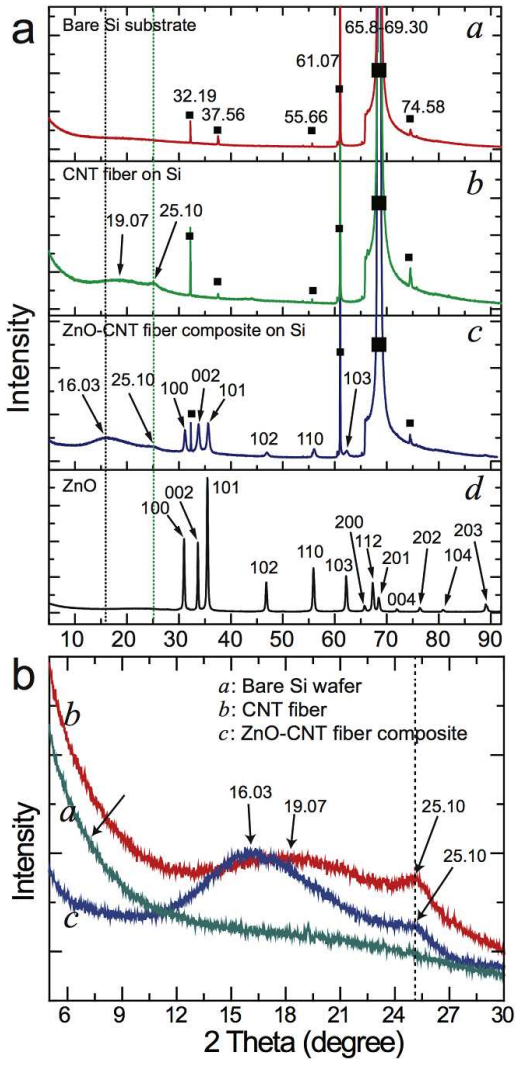

Fig. 5. (a) XRD spectra of *a* bare Si wafer substrate, *b* the as-synthesized CNT fiber on the Si wafer, *c* the ZnO–CNT fiber composite on the Si wafer, and *d* the pure ZnO nanoparticles, respectively. (b) The peak position was elucidated by collecting magnified spectra over the region 5–30° (curve *a*) for the Si wafer, (curve *b*) for the CNT fibers on the Si wafer, and (curve *c*) for the ZnO–CNT fiber composites on the Si wafer.

to an as-synthesized silicon substrate (curve 5a*a*). Curve 5a*c* corresponded to the XRD spectrum of a ZnO–CNT fiber composite with carbon peaks at 16.03 and 25.10. The other peaks were attributed to the ZnO planes. All ZnO peaks were consistent with a hexagonal wurtzite structure in the ZnO nanoparticles of the JCPDS no. 01-075-0576 [25]. The peaks corresponding to the 100, 002, 101, 102, and 103 planes of ZnO were observed in the XRD spectrum of the ZnO–CNT fiber composite but peaks corresponding to the 200, 112, 201, 004, 202, 104, and 202 planes were not observed due to the high intensity peaks derived from the Si substrate. The XRD peaks corresponding to ZnO indicated that the ZnO nanoparticles of the composite assumed a hexagonal crystalline wurtzite structure.

The carbon peaks in curve 5(b)*c* were shifted to 16.03 from 19.07, indicating that the ZnO nanoparticles interacted with the poorly crystalline carbon. It is possible that ZnO intercalated between the walls of the multiwall

CNTs or chemically bonded to the CNT surfaces through oxygen containing groups that formed Zn–O–CNT and Zn–OOC-CNT structures. Intercalation or chemical bonding was possible among the poorly crystalline carbon. The spectrum around the carbon peaks was magnified (panel 5(b)) to reveal that the poorly crystalline carbon peak shifted from 19.07 to 16.03 while the crystalline carbon peak (25.10) remained fixed in the as-synthesized CNT fibers and ZnO–CNT fiber composites.

The Raman spectra supported the presence of defect carbon atoms, which facilitated intercalation or chemical bonding between ZnO and the CNTs. The D band in the Raman spectrum of the CNT fiber (Fig. 6a) indicated the presence of structural carbon defects in the CNT fibers. The D band may have been due to the presence of oxygen containing functional groups or missing conjugation systems. The Raman peaks at 96.08, 429.38, and 561.2 cm^{-1} in curve c corresponded to E_2 (low) [29], E_2 (high) [30], and $A1$–LO (longitudinal optical) [29] phonons in the ZnO nanoparticles of the ZnO–CNT fiber composite. These were also observed in curve a for the pure ZnO nanoparticles. The peak at 221.6 was assigned to a second-order Raman intensity arising from the zone boundary (M point) phonon 2–$E_2(M)$. This peak is normally found around 205–208 cm^{-1} [31, 32], but in the ZnO–CNT fiber composites it was blue-shifted due to the higher energy of ZnO as indicated by curve a. The peak at 322.4 cm^{-1} corresponded to a multiple phonon scattering process [32]. The $A1$–LO phonon peak (561.2 cm^{-1}) was blue-shifted from 574, 576 cm^{-1} [29], and 579 cm^{-1} [33], owing to the strong interaction between ZnO and the carbon atoms of the CNT fiber. The observation of a peak at 561.2 cm^{-1} corresponding to the $A1$–LO mode was close to the theoretically predicted value (548 cm^{-1}) [34].

Interestingly, a radial breathing mode (RBM) of the CNTs in the ZnO–CNT fiber composites was observed at 181.7 cm^{-1}. This mode was not observed in the as-synthesized CNTs (curve b). These results indicated that the RBM mode was activated by the interaction between the ZnO nanoparticles and the CNTs through chemical bonds which influenced the radial polarization of the CNTs. This interaction may occur if ZnO vibrates in the radial direction. The RBM is not readily enhanced by the surface deposition of ZnO nanoparticles without chemical bond formation.

Curve c revealed that the D, G, and $2D$ bands were blue-shifted by 3.7, 6.7, and 13.2 cm^{-1}, respectively. These shifts were clearly observed in the magnified spectra (Fig. 4d–f) over the regions 1250–2800, 1250–1700, and 2500–2800 cm^{-1}, respectively. Similarly, the ZnO peaks in the ZnO–CNT fiber composite revealed that the E_2 (high) and $A1$–LO phonon modes shifted to 429.3 and 561.2 cm^{-1} (curve c in Fig. 6b) from 432.3 and 570.0 cm^{-1} (curve a in Fig. 6b), respectively. The vibrational shifts in the D, G, $2D$, E_2 (high), and $A1$–LO phonon modes and the high-intensity RBM in the ZnO–CNT fiber composite supported the presence of chemical

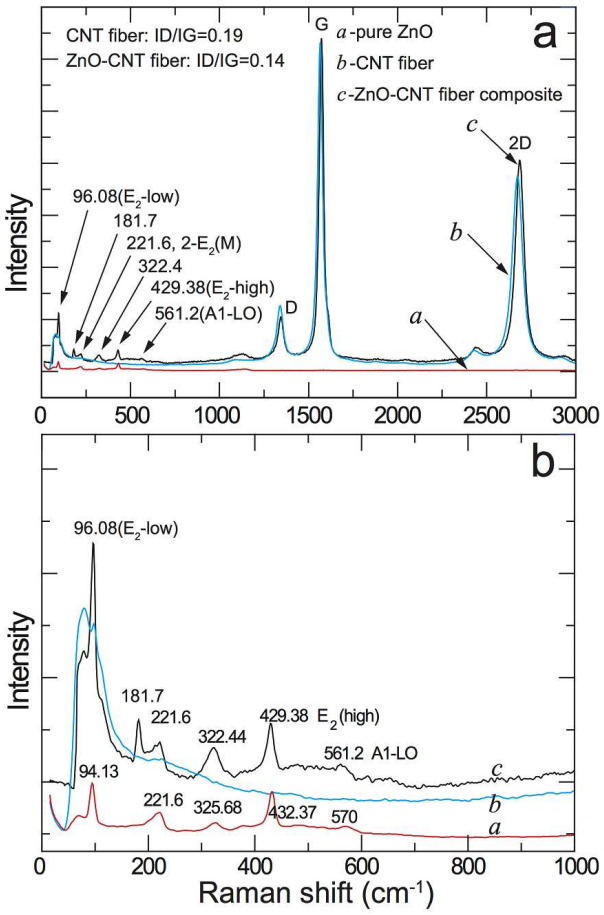

Fig. 6. (a) Raman spectra of (curve a) pure ZnO, (curve b) CNT fibers, and (curve c) ZnO–CNT fiber composites, respectively. (b) The peak positions were elucidated by collecting the magnified spectra over the region 0–1000 cm^{-1} for (a).

bonds at the interface between the CNT fibers and the ZnO nanoparticles. The Raman spectrum was collected from the *ex situ* prepared ZnO–CNT fiber composites (Fig. 4c). This spectrum presented no RBM and no significant shifts in the D, G, and $2D$ bands of the CNTs in the ZnO–CNT fiber composites. These features indicated a lack of significant interactions or chemical bonds at the interface between the CNTs and ZnO as a result of the *ex situ* process.

The inner sides of the ZnO–CNT fiber composites were analyzed using FIB cuts. Figure 7a shows a cross-sectional SEM image of a ZnO–CNT fiber composite, revealing ribbon-like fibers with a folded edge. The upper region (marked by a dotted line, area-3) was damaged by the Ga ion beam. An SEM image taken from area-2 is shown in Fig. 7b, revealing the presence of ZnO nanoparticles (marked by arrows) on the CNT surface. The rectangular region in Fig. 7b is displayed in Fig. 7c and also reveals ZnO nanoparticles on the CNT fiber surface. The middle portion of the cross-sectional cut area-1 is shown in Fig. 7d. This area reveals ZnO nanoparticles

(some of them are marked by arrows). ZnO nanoparticles were also found in the folded portions of the ZnO–CNT fiber composites (Fig. 7e). The inner side was analyzed by EDX mapping (Fig. 7f) to visualize the presence of Zn, O, and C elements. The inset of Fig. 7f was collected from the inner side and an analysis of the rectangular region revealed the presence of ZnO nanoparticles inside of the CNT fibers.

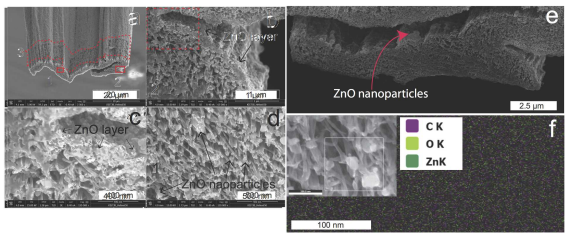

Fig. 7. (a) Cross-sectional cut of the ZnO–CNT fiber composites obtained using the FIB technique. (b)–(d) SEM images collected from the regions marked 2 (rectangle), 3 (dotted line), or 1 (rectangle) for (a). (e) SEM image of the folded part at the bottom of (a), revealing the presence of ZnO nanoparticles. (f) EDX mapping of the square region indicated in the inset of the SEM image of the ZnO–CNT fiber composite. The C, O, and Zn elements in the mapping are indicated in purple, light green, and dark green, respectively.

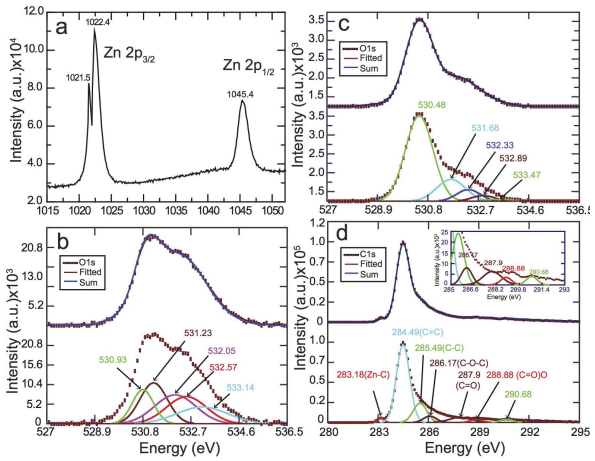

Fig. 8. XPS spectra of the ZnO–CNT fiber composite for (a) Zn-$2p_{3/2}$ and $2p_{1/2}$, (b) and (c) O-1*s* in the *in situ*- and *ex situ*-prepared samples, respectively, and (d) C-1*s*.

The characteristics of the ZnO bond with the CNT fibers were analyzed by XPS (Fig. 8). Peaks corresponding to $2p_{3/2}$ and $2p_{1/2}$ (Fig. 8a) were observed at 1022.4 and 1045.4 eV, respectively, and were attributed to Zn in an oxidation state consistent with ZnO. The shoulder peak at 1021.5 eV for Zn$2p_{3/2}$ suggested that the ZnO–CNT fiber composite contained significant free nonoxidized Zn [35]. These results indicated that ZnO nanoparticles in the ZnO–CNT fiber composite contained oxygen vacancy defects. The O1*s* peak (Fig. 8b) could be decomposed into several components at 530.93, 531.23, 532.05, 532.57, 533.14 eV and their convolution fit well to the O1*s* curve (the upper curve). The low energy peak at 530.93 eV corresponded to O^{-2} in the wurtzite structure of the ZnO lattice. The peaks at 531.23 and 532.05 eV were related to O^{-2} moieties in the oxygen deficient region within the ZnO matrix [36]. The high-energy peak at 532.57 eV originated from a C=O functional group bonded to Zn in the poorly crystalline carbon atoms of CNT [37]. The highest energy peak at 533.14 eV originated from a C–O functional group [38]. Oxygen vacancy defects typically appear as one peak, but the ZnO–CNT fiber composite displayed two peaks at 531.23 and 532.05 eV. The higher electronegativity of carbon relative to Zn could play a role in providing two peaks. Carbon could be chemically bonded to Zn to form C–Zn–C (531.23 eV) or –O–Zn–C (532.05 eV) groups at oxygen deficient sites. Thus the peaks observed at 532.57 and 533.14 eV could have been due to the more electronegative oxygen environment [39]. Carbon could have been indirectly bonded to Zn to form –O–Zn–O–C via the oxygen in C–O or C=O functional groups producing a more oxygen-rich environment. The peak at 531.23 eV was more intense than the other peaks, indicating the creation of a significant number of oxygen vacancy defects in ZnO.

The *ex situ* prepared ZnO–CNT fiber composite was analyzed using XPS (Fig. 8c) and the peaks are summarized in Table I in comparison with the peaks obtained from the *in situ* prepared composite. The intensity of peaks 1 and 3–5 in the *ex situ* composite were less intense than those obtained from the *in situ* composite. The binding energies for peaks 1, 3, and 4 were lower in the *ex situ* composite. The low intensity and low binding energy suggested a weaker interaction between ZnO and the CNTs in the *ex situ* ZnO–CNT fiber composites. The intensity of peak 2 (due to the C–Zn–C bond) was insignificant in the *ex situ* composite, also due to the weak interactions between ZnO and carbon. Note that no RBM was observed in the Raman spectra (Fig. 4c) of the *ex situ* composite. These XPS features indicated the presence of a chemical interaction (or chemical bonding) in the *in situ* composite, consistent with the Raman analysis.

The deconvoluted curves of the C1*s* XPS spectra obtained from the ZnO–CNT fiber composite are displayed in Fig. 6d. Several peaks corresponded to binding energies of 284.49, 285.49, 286.17, 287.9, 288.88, and 290.68 eV associated with the C=C bond of the sp^2 carbon, the C–C bond of the sp^3 amorphous carbon, C–O–C, C=O, and (C=O)O, respectively [40]. A $\pi - \pi^*$ transition in the C=C network of the ZnO–CNT fiber composite was observed at 290.68 eV. The low-energy peak at 283.18 eV was attributed to a chemical bond between Zn and C, for example, Zn–C [41]. The peaks corresponding to C1*s* also supported the presence of oxygen containing functional groups in the CNTs of the ZnO–CNT fiber composite as in the Raman and O1*s* XPS spectra.

The light absorption properties of the ZnO–CNT fiber composite were investigated by measuring the UV-visible near-IR spectra (Fig. 9b). The ZnO–CNT fiber composite (Fig. 9a) was carefully transferred to a quartz glass substrate (Fig. 9b). Pristine CNT fibers were prepared for comparison. The spectra of the ZnO–CNT fiber composite and pristine CNT fibers are presented in Fig. 10a. Stronger light absorption was observed in the ZnO–CNT fiber composite throughout the whole 300–2100 nm range as compared to the pristine CNT fiber. The ZnO absorption band in the composite was observed at 382 nm, slightly higher than that of the pure ZnO (362 nm, Fig. 9c). The enhanced absorption of the ZnO–CNT fiber composite may have been due to chemical bonds between the Zn and carbon [41], oxygen vacancy defects in the presence of the Zn *d-d* transition [36], carbon doping of the ZnO nanoparticles [42], or multiple light scattering [43] by the ZnO nanospheres (as shown in Fig. 2).

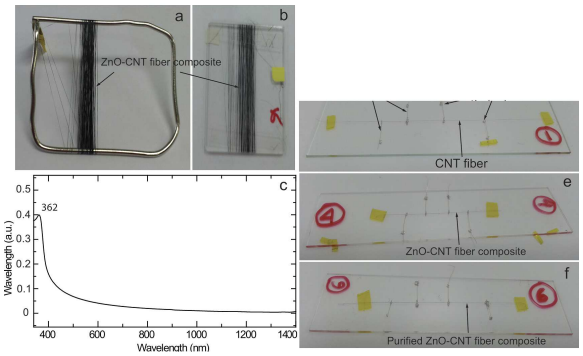

Fig. 9. (a) and (b) ZnO–CNT fiber composite was transferred to a quartz glass substrate. (c) UV-visible near-IR spectra pure ZnO. (d)–(f) The electrical conductivity CNT fiber, ZnO–CNT fiber composite, and purified ZnO–CNT fiber composite, respectively.

TABLE I

XPS O-1*s* peak positions, binding energies E_b, and intensities of the *in situ* and *ex situ* prepared ZnO–CNT.

	in situ		*ex situ*	
Peak	E_b [eV]	Intensity	E_b [eV]	Intensity
1	530.93	≈9000	530.48	3500
2	531.23	10500	–	–
3	532.05	7700	531.68	1880
4	532.57	7500	532.33	1600
5	533.14	4300	533.47	1300

The effects of the ZnO nanoparticles on the thermal stabilities of the ZnO–CNT fiber composites were tested using thermogravimetric analysis (TGA) at a heating rate of 10 °C/min under an N_2 atmosphere. The TGA curves obtained from the ZnO–CNT fiber composites, pristine CNT fibers, and ZnO nanoparticles are displayed in Fig. 7b. Significant thermal degradation of the pure ZnO was not observed until 880 °C, but the pristine CNT fibers slowly degraded from 100 to 540 °C. A dramatic degradation of the pristine CNT fibers occurred above 540 °C, and the CNT fibers were 74% degraded at 880 °C. On the other hand, no significant weight loss was observed in the ZnO–CNT fiber composites over the range 100–540 °C. As the temperature increased from 540 °C to 880 °C, slow weight loss was observed. A degradation of 26% occurred, corresponding to nearly one-third of the pristine CNT fibers. Our TGA analysis revealed that the prepared ZnO–CNT fiber composite was more thermally stable than the pristine CNT fibers. ZnO nanoparticles on the CNT fiber surface could work as a protective layer against thermal decomposition.

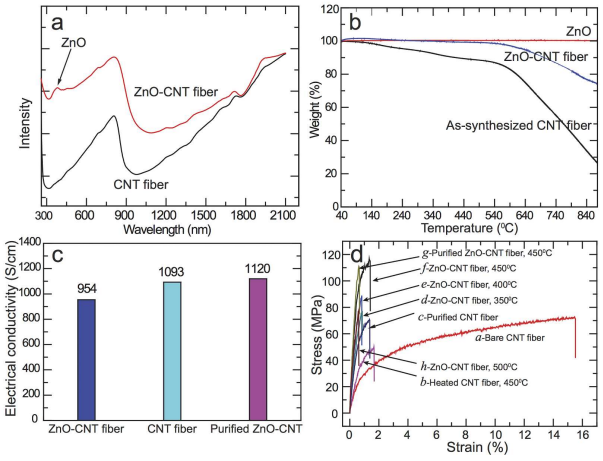

Fig. 10. (a) UV-vis NIR spectra of the as-synthesized CNTs and ZnO–CNT fiber composites, respectively. (b) Thermogravimetric analysis of the pure ZnO, CNT fibers, and ZnO–CNT fiber composites, respectively. (c) Electrical conductivities of the as-synthesized CNTs and as-prepared and purified ZnO–CNT fiber composites, respectively. (d) Mechanical properties (stress vs. strain curves) of the CNTs and ZnO–CNT fiber composites prepared under various conditions. Curve *a* — as-synthesized CNT fibers, curve *b* — CNT fibers heated at 450 °C for 20 min, curve *c* — purified CNT fibers, curves *d*–*h* — ZnO–CNT fiber composites prepared at 350 °C, 400 °C, 450 °C, and 500 °C for 20 min, respectively, and curve *g* — the purified ZnO–CNT fiber composites prepared at 450 °C.

The electrical conductivities of the ZnO–CNT fiber composite and pristine CNT fibers were measured. Because ZnO is a semiconductor, a decrease in the electrical conductivity of the CNT fiber composite was expected. The measurement scheme is displayed in Fig. 9d–9f. CNT fibers (Fig. 9d), ZnO–CNT fiber composites (Fig. 9e), and purified CNT composite fibers (Fig. 9f) were prepared on a glass slide using gold wires and silver paste. The sample was placed under a microscope to connect four needles (Fig. 11b) to the corresponding points (Fig. 11c) with the help of a microscope. A source meter and multimeter were used to measure the output voltage under application of a 105 µA current to the source meter. The four points (marked 1–4 in Fig. 11c) of the CNT

Fig. 11. (a)–(c) CNT fiber was placed under a microscope to connect four needles to the corresponding points with the help of a microscope. (d) A source meter and multimeter were used to measure the output voltage under application of a 105 µA current to the source meter. The four points (marked 1–4 in (c)) of the CNT fiber were connected to the source meter and the multimeter's corresponding points (marked 1–4 in (d)).

fiber were connected to the source meter and the multimeter's corresponding points (marked 1–4 in Fig. 11d). The output voltage between points 2 and 3 was converted to the corresponding resistance (R), and the calculated resistance was converted to the resistivity (ρ). The electrical conductivity was calculated to be $\sigma = 1/\rho = l/AR$, where A is the cross-sectional area of the CNT fiber, and l is the length of the CNT fiber between points 2 and 3. The average electrical conductivities of the pristine CNT fibers (1093 S/cm), ZnO–CNT fiber composites (954 S/cm), and purified ZnO–CNT fiber composites (1120 S/cm) were calculated (Fig. 10c). The electrical conductivity of the ZnO–CNT fiber composite remained very high, indicating that the ZnO deposition did not significantly affect the conductivity due to direct and indirect chemical bonds between Zn and C. Free Zn may form a conductive path between CNTs through the chemical bonds (Zn–C, C–Zn–C, O–Zn–C, Zn–O–C, or Zn–Zn–C) involving oxygen vacancies of ZnO. The ZnO–CNT fiber composite prepared using purified CNT fibers displayed a slightly enhanced electrical conductivity (1120 S/cm) compared to that of the ZnO–CNT composite and the pristine CNT fibers.

TABLE II

Mechanical properties of the CNTs and ZnO–CNT fiber composites prepared under various conditions.

Materials	Fabrication condition (20 min)	Strain [%]	Stress [MPa]	Young modulus [GPa]
pristine CNT fiber	no treatment	16.6±2.2	75.6±4.1	4.7±0.6
ZnO–CNT fiber	350 °C	1.43±1.07	81.01±24.50	12.17±3.31
ZnO–CNT fiber	400 °C	1.2±1.0	93.2±28.6	15.6±3.85
ZnO–CNT fiber	450 °C	1.09±0.27	117.7±15.4	19.8±4.1
ZnO–CNT fiber	500 °C	0.52±0.19	76.74±5.0	21.6±3.5
purified CNT fiber	—	1.2±0.4	70.8±9.2	9.2±3.5
purified ZnO–CNT fiber	450 °C	0.65±0.30	111.0±20.4	21.2±3.2
pristine CNT fiber	450 °C	1.19±0.50	46.76±10.0	6.59±1.1

The mechanical properties of the ZnO–CNT fiber composites produced at different temperatures (30–500 °C) were investigated (Fig. 10d and Table II) ZnO–CNT fiber composites prepared from 350–450 °C exhibited an enhanced Young modulus, which increased from 4.7 to 19.8 GPa and stress values that increased from 75.6 to 117.7 MPa. The ZnO–CNT fiber composite prepared at 500 °C displayed a slightly higher Young modulus (21.6 GPa) although its stress (76 MPa) was lower than that obtained at 450 °C (as-prepared). The pristine CNT fiber heated at 450 °C exhibited a low stress of 46.76 MPa and a slight increase in the Young modulus (6.59 GPa) compared to the non-heated pristine CNT fibers. Purification of the CNTs prior to producing the composite did not improve the mechanical properties of the ZnO–CNT fiber composite. This observation suggested that thermal heating of the purified CNTs did not significantly improve the mechanical properties of the ZnO–CNT fiber composite. Chemical bonds between Zn and carbon were attributed to the enhanced mechanical properties of the ZnO–CNT fiber composite.

4. Conclusion

The simple deposition of ZnO nanoparticles onto the CNT fiber surface via an *in situ* solution process provided a high electrical conductivity and a high Young modulus for the ZnO–CNT fiber composites. A low temperature of 450 °C was sufficient to prepare ZnO nanoparticles homogeneously deposited onto the CNT fiber surfaces as well as in the gaps of individual CNTs (inside of the CNT fibers). Strong interactions between the CNTs and ZnO nanoparticles were produced in the present *in situ* process, attributed to chemical bonds involving Zn and defect sites on the CNTs. The strong interactions enabled efficient thermal protection of the CNT fibers at temperatures up to 880 °C and produced a conductive pathway that maintained the high electrical conductivity (954–1120 S/cm). An enhanced load bearing capacity and light absorption properties from the UV-visible to the near-IR regions could have resulted from oxygen vacancy defects and light scattering by the ZnO nanoparticles chemically bonded to the carbon atoms.

Acknowledgments

This work was supported by grant from the Korean government (NRF-2015R1D1A1A-09059647). M.M.H. was supported by BK21 PLUS program.

References

[1] J. Bae, M.K. Song, Y.J. Park, J.M. Kim, M. Liu, Z.L. Wang, *Angew. Chem. Int. Ed.* **50**, 1683 (2011).

[2] Y. Fu, X. Cai, H. Wu, Z. Lv, S. Hou, M. Peng, X. Yu, D. Zou, *Adv. Mater.* **24**, 5713 (2012).

[3] S. Pan, Z. Yang, P. Chen, X. Fang, G. Guan, Z. Zhang, J. Deng, H. Peng, *J. Phys. Chem. C* **118**, 16419 (2014).

[4] X. Xiao, T. Li, P. Yang, Y. Gao, H. Jin, W. Ni, W. Zhan, X. Zhang, Y. Cao, J. Zhong, L. Gong, W.-C. Yen, W. Mai, J. Chen, K. Huo, Y.-L. Chueh, Z.L. Wang, J. Zhou, *ACS Nano* **6**, 9200 (2012).

[5] J. Ren, L. Li, C. Chen, X. Chen, Z. Cai, L. Qiu, Y. Wang, X. Zhu, H. Peng, *Adv. Mater.* **25**, 1155 (2013).

[6] Y. Meng, Y. Zhao, C. Hu, H. Cheng, Y. Hu, Z. Zhang, G. Shi, L. Qu, *Adv. Mater.* **25**, 2326 (2013).

[7] F. Vollrath, D.P. Knight, *Nature* **410**, 541 (2001).

[8] Z. Xu, C. Gao, *Macromolecules* **43**, 6716 (2010).

[9] W. Kylberg, F.A.D. Castro, P. Chabrecek, U. Sonderegger, B.T.T. Chu, F. Nüesch, R. Hany, *Adv. Mater.* **23**, 1015 (2011).

[10] J.A. Lee, M.K. Shin, S.H. Kim, H.U. Cho, G.M. Spinks, G.G. Wallace, M.D. Lima, X. Lepró, M.E. Kozlov, R.H. Baughman, S.J. Kim, *Nat. Commun.* **4**, 1970 (2013).

[11] K. Wang, Q. Meng, Y. Zhang, Z. Wei, M. Miao, *Adv. Mater.* **25**, 1494 (2013).

[12] N. Behabtu, C.C. Young, D.E. Tsentalovich, O. Kleinerman, X. Wang, A.W.K. Ma, E.A. Bengio, R.F.T. Waarbeek, J.J.D. Jong, R.E. Hoogerwerf, S.B. Fairchild, J.B. Ferguson, B. Maruyama, J. Kono, Y. Talmon, Y. Cohen, M.J. Otto, M. Pasquali, *Science* **339**, 182 (2013).

[13] H. Sun, X. You, J. Deng, X. Chen, Z. Yang, J. Ren, H. Peng, *Adv. Mater.* **26**, 2868 (2014).

[14] H. Zhang, G. Cao, Z. Wang, Y. Yang, Z. Shi, Z. Gu, *Nano Lett.* **8**, 2664 (2008).

[15] C. Yuan, X. Zhang, L. Su, B. Gao, L. Shen, *J. Mater. Chem.* **19**, 5772 (2009).

[16] C.-C. Hu, K.-H. Chang, M.-C. Lin, Y.-T. Wu, *Nano Lett.* **6**, 2690 (2006).

[17] Z. Chen, V. Augustyn, J. Wen, Y. Zhang, M. Shen, B. Dunn, Y. Lu, *Adv. Mater.* **23**, 791 (2011).

[18] J.G. Ok, J.Y. Lee, H.W. Baac, S.H. Tawfick, L.J. Guo, A.J. Hart, *ACS Appl. Mater. Interfaces* **6**, 874 (2014).

[19] C.H. Hsu, H.Y. Liao, P.L. Kuo, *J. Phys. Chem. C* **114**, 7933 (2010).

[20] B. Wu, D. Hu, Y. Kuang, B. Liu, X. Zhang, J. Chen, *Angew. Chem. Int. Ed.* **48**, 4751 (2009).

[21] D. Wang, S. Lu, S.P. Jiang, *Electrochim. Acta* **55**, 2964 (2010).

[22] E. Lorençon, A.S. Ferlauto, S.D. Oliveira, D.R. Miquita, R.R. Resende, R.G. Lacerda, L.O. Ladeira, *ACS Appl. Mater. Interfaces* **1**, 2104 (2009).

[23] S. Guo, X. Pan, H. Gao, Z. Yang, J. Zhao, X. Bao, *Chem. Eur. J.* **16**, 5379 (2010).

[24] A. Zamudio, A.L. Elías, J.A. Rodríguez-Manzo, F. López-Urías, G. Rodríguez-Gattorno, F. Lupo, M. Rühle, D.J. Smith, H. Terrones, D. Díaz, M. Terrones, *Small* **2**, 346 (2006).

[25] M.M. Hossain, A.H.A. Mamun, J.R. Hahn, *J. Phys. Chem. C* **116**, 23153 (2012).

[26] H. Shima, M.M. Hossain, J.R. Hahn, *RSC Adv.* **4**, 41204 (2014).

[27] Y. Bu, Z. Chen, W. Li, B. Hou, *ACS Appl. Mater. Interfaces* **5**, 12361 (2013).

[28] J. Lee, Y. Jung, J. Song, J.S. Kim, G.-W. Lee, H.J. Jeong, Y. Jeong, *Carbon* **50**, 3889 (2012).

[29] B.H. Bairamov, A. Heinrich, G. Irmer, V.V. Toporov, E. Ziegler, *Phys. Status Solidi B* **119**, 227 (1983).

[30] D.I. Son, B.W. Kwon, D.H. Park, W.S. Seo, Y. Yi, B. Angadi, C.-L. Lee, W.K. Choi, *Nat. Nanotechnol.* **7**, 465 (2012).

[31] M. Rajalakshmi, A.K. Arora, B.S. Bendre, S. Mahamuni, *J. Appl. Phys.* **87**, 2445 (2000).

[32] J.M. Calleja, M. Cardona, *Phys. Rev. B* **16**, 3753 (1977).

[33] C.A. Arguello, D.L. Rousseau, S.P.S. Porto, *Phys. Rev.* **181**, 1351 (1969).

[34] A. Zaoui, W. Sekkal, *Phys. Rev. B* **66**, 174106 (2002).

[35] T. Ohshima, Y. Murakami, H. Kawasaki, Y. Suda, Y. Yagyu, *Jpn. J. Appl. Phys.* **50**, 8S1 (2011).

[36] J. Wang, Z. Wang, B. Huang, Y. Ma, Y. Liu, X. Qin, X. Zhang, Y. Dai, *ACS Appl. Mater. Interfaces* **4**, 4024 (2012).

[37] Y. Lv, L. Yu, H. Huang, Y. Feng, D. Chen, X. Xie, *Nanotechnology* **23**, 065402 (2012).

[38] M. Salavati-Niasari, F. Davar, M. Bazarganipour, *Dalton Trans.* **39**, 7330 (2010).

[39] K. Jayanthi, M. Sunkara, S. Chawla, *J. Phys. D Appl. Phys.* **46**, 325101 (2013).

[40] C.-C. Teng, C.-C.M. Ma, C.-H. Lu, S.-Y. Yang, S.-H. Lee, M.-C. Hsiao, M.-Y. Yen, K.-C. Chiou, T.-M. Lee, *Carbon* **49**, 5107 (2011).

[41] Y.-P. Zhu, M. Li, Y.-L. Liu, T.-Z. Ren, Z.-Y. Yuan, *J. Phys. Chem. C* **118**, 10963 (2014).

[42] X. Zhou, Y. Li, T. Peng, W. Xie, X. Zhao, *Mater. Lett.* **63**, 1747 (2009).

[43] Q. Zhang, T.P. Chou, B. Russo, S.A. Jenekhe, G. Cao, *Adv. Funct. Mater.* **18**, 1654 (2008).